Science Advances
AAAS

advances.sciencemag.org/cgi/content/full/7/21/eabg0942/DC1

# Supplementary Materials for

## Receptor compaction and GTPase rearrangement drive SRP-mediated cotranslational protein translocation into the ER

Jae Ho Lee, Ahmad Jomaa*, SangYoon Chung, Yu-Hsien Hwang Fu, Ruilin Qian, Xuemeng Sun, Hao-Hsuan Hsieh, Sowmya Chandrasekar, Xiaotian Bi, Simone Mattei, Daniel Boehringer, Shimon Weiss, Nenad Ban*, Shu-ou Shan*

*Corresponding author. Email: sshan@caltech.edu (S.S.); ban@mol.biol.ethz.ch (N.B.); ahmad.jomaa@mol.biol.ethz.ch (A.J.)

Published 21 May 2021, *Sci. Adv.* **7**, eabg0942 (2021)
DOI: 10.1126/sciadv.abg0942

**This PDF file includes:**

**Supplementary Methods**

***Preprotein targeting and translocation assays.***

Co-translational targeting and translocation of $^{35}$S-methionine labeled pPL into salt-washed, trypsinized rough ER microsome (TKRM) (*5*, *43*) were carried out as outlined in fig. S1A. Unless otherwise specified, translocation reactions contained 20 nM SRP (when [SR] is varied), 100 nM SR (when [SRP] is varied), and 0.5 eq of TKRM (as defined in (*68*)). The reactions in fig. S1 contained 7-Me-GTP, and 7-Me-GTP was omitted for the reactions shown in Fig. 6 and fig. S10. Translocation efficiency was quantified as:

$$\text{Fraction Translocation} = \frac{(8/7)\text{prolactin}}{(8/7)\text{prolactin} + \text{preprolactin}}$$

The (8/7) term corrects for the difference in the number of methionines in preprolactin and signal-sequence cleaved prolactin.

***Measurement of GTPase rate constants.***

Basal GTPase reactions were measured under single-turnover conditions using varying concentrations of SRP54 in excess of γ-$^{32}$P-GTP. The SRP54 concentration dependence of the observed rate constant ($k_{obsd}$) were fit to Eq. 1,

$$k_{obsd} = k_{cat} \times \frac{[SRP]}{K_m + [SRP]} \qquad (1)$$

in which $k_{cat}$ is the basal GTPase rate constant at saturating SRP concentrations, and $K_m$ is the GTP concentration required to reach half of $k_{cat}$.

The reciprocally stimulated GTPase reaction between SRP and SR were measured under multiple turnover conditions using 0.2 μM SRP, varying concentrations of SR in excess of SRP, and 100 μM GTP (or 500 μM GTP for mutant SRP(G226E)) doped with trace γ-$^{32}$P-GTP. All

reactions were measured in the targeting complex in which SRP was bound to the signal sequence and ribosome. The SR concentration dependences of the observed rate constants were fit to Eq. 2.

$$k_{obsd} = k_{cat} \times \frac{[SR]}{K_m + [SR]} \qquad (2)$$

As shown in Lee et. al (*5*), the value of $k_{cat}/K_m$ is rate-limited by and therefore reports on the SRP-SR complex assembly rate constant.

***Steady state fluorescence measurements.***

Steady state fluorescence was measured using a Fluorolog 3-22 Spectrofluorometer (Horiba Jobin Yvon) following manufacturer's guidelines. To monitor the effects of SR, fluorescence emission spectra were recorded for 15 nM SRP-4A10L singly labeled with the indicated fluorescent dyes at specified positions, in the presence of 100 nM 80S with and without 1.5 μM SR present (fig. S2G-S2J). To monitor the effects of SRP, fluorescence emission spectra were recorded for 30 nM SR singly-labeled labeled with the indicated fluorescent dyes at specified positions, in the presence of 400 nM 80S with and without 400 nM SRP-4A10L present (fig. S2K-S2L). To monitor the effects of 80S, fluorescence emission spectra were recorded for singly labeled SRP-4A10L or SR in the absence and presence of 100 nM (for Proximal and Distal probes) or 400 nM (for Compaction probes) 80S (fig. S2M-S2P). All reactions also contained 200 μM GppNHp and 0.6 mg/ml BSA.

Fluorescence anisotropy was measured using the anisotropy module on Fluorolog 3-22 following the manufacturer's guidelines. The reaction contained 15 nM SRP-4A10L or 30 nM SR labeled with the indicated fluorescent dyes at specified positions (fig. S2A and S2R), 200 μM

GppNHp, 0.6 mg/ml BSA, and 100 nM/400 nM 80S (for Distal/Compaction probes, respectively) where indicated.

The $K_d$ values of the SRP•SR and SRP•SRΔMoRF complexes were determined by equilibrium titrations. Titration of the SRP•SR complex used 15 nM SRP labeled with Cy3B at SRP54 C47, 200 nM RNC with a 4A10L signal sequence, and indicated concentrations of SR labeled with Atto647N at the C-terminus of SRα (*5*). Titration of the SRP·SRΔMoRF complex used 15 nM SRP with SRP54 fused to the 4A10L signal sequence (SRP-4A10L) and labeled with Cy3B at SRP54 C47, 50 nM purified 80S ribosome, and indicated concentrations of Atto647N labeled SR. The combination of signal sequence fusion to SRP54 and 80S ribosome has the same effect as RNC on SRP-SR binding kinetics and stability (*5*). SR also contained the R458A mutation to block GTP hydrolysis and hydrolysis-driven dissociation of the SRP•SR complex (*5*). 0.6 mg/ml BSA was supplemented in SRP Assay buffer to reduce non-specific adhesion of proteins to surfaces. A control titration with unlabeled SR was carried out in parallel, and the fluorescence intensity change from the control reaction was subtracted from that of the reaction with Atto647N-labeled SR. FRET efficiency (E) at each SR concentration were calculated as $E = 1 - \frac{F_{DA}}{F_D}$, in which $F_{DA}$ and $F_D$ are the fluorescence signals with and without the acceptor dye present, respectively. Values of E were plotted against SR concentration and fit to Eq. 3

$$E = E_{max} \times \frac{[SRP]+[SR]+K_d-[\sqrt{([SRP]+[SR]+K_d)^2-4\times[SRP]\times[SR]}}{2\times[SRP]} \qquad (3)$$

in which $E_{max}$ is the FRET efficiency of the SRP·SR complex observed at saturating SR concentrations.

The binding of $SRP_{G226E}$ to SR and SRΔMoRF were measured by using unlabeled SR or SRΔMoRF as competitive inhibitors of the FRET between Cy3B-labeled $SRP_{G226E}$ and Atto647N-labeled SR. 15 nM $SRP_{G226E}$-4A10L-Cy3B, 50 nM 80S ribosome and 50 nM SR-Atto647N were pre-incubated to reach equilibrium. Unlabeled SR (WT or ΔMoRF) was titrated to compete with SR-Atto647N for binding to $SRP_{G226E}$. The donor fluorescence intensity (F) was normalized and fit to Eq. 4:

$$F = \frac{[SR]}{K_i \times \left(1 + \frac{[SR*]}{K_{d,SR*}}\right) + [SR]} \qquad (4)$$

in which $K_i$ is inhibition constant of unlabeled SR and equals the $K_d$ of the $SRP_{G226E}$•SR or $SRP_{G226E}$•SRΔMoRF complex, [SR*] is the concentration of SR-Atto647N (50 nM). $K_{d,SR*}$ is the $K_d$ value of the labeled $SRP_{G226E}$•SR-Atto647n complex and was calculated from the $k_{on}$ and $k_{off}$ values of this complex (Fig. 3A and 3B).

Rate constants for association of SRP and $SRP_{G226E}$ with SR were measured using SRP labeled with Cy3B at SRP54(C47) and SR was labeled with Atto647N at the C-terminus of SRα-NG. 15 nM SRP-4A10L-Cy3B or $SRP_{G226E}$-4A10L-Cy3B were rapidly mixed with indicated concentrations of SR-Atto647N on a stopped-flow apparatus (Kintek). 50 nM 80S ribosome was pre-incubated with SRP prior to initiation of the reaction. Observed rate constants of SRP-SR association ($k_{obsd}$) were determined as a function of SR concentration and fit to Eq. 5,

$$k_{obsd} = k_{off} + k_{on}\,[SR] \qquad (5)$$

in which $k_{on}$ is the association rate constant.

Dissociation rate constants of the targeting complex were measured using pulse-chase experiments. 15 nM SRP-4A10L-Cy3B or $SRP_{G226E}$-4A10L-Cy3B, 50 nM 80S ribosome and 50 nM SR-Atto647N were pre-incubated to reach equilibrium. A 10-fold excess of unlabeled SR was added to initiate complex dissociation, and the time courses of the fluorescence trace were

recorded on the stopped-flow. For $SRP_{G226E}$, the time trace of observed fluorescence intensity (F) were fit to a single exponential function (Eq. 6),

$$F = F_0 + \Delta F \times e^{-kt} \quad (6)$$

In which $F_0$ is the fluorescence intensity at t = 0, ΔF is the fluorescence change when the reaction reached equilibrium, and *k* is the dissociation rate constant. For SRP, the time trace of observed fluorescence intensity (F) was biphasic and fit to Eq. 7,

$$F = F_0 + \Delta F_{fast} \times e^{-k_{fast}t} + \Delta F_{slow} \times e^{-k_{slow}t} \quad (7)$$

Rate constants of conformational changes in the targeting complex were measured using the stopped-flow by rapidly mixing 15 nM SRP-4A10L labeled with Proximal (Detachment) or Distal (Distal docking) probes with varying concentrations of unlabeled SR. The reactions also contained 40 nM 80S, 200 μM GppNHp, and 0.6 mg/ml BSA. The time courses of donor fluorescence intensity change were fit to Eq 6 to extract the observed rate constants ($k_{obsd}$). The SR concentration dependences of $k_{obsd}$ were fit to Eq. 2 to obtain the rate constant at saturation, which is not limited by bi-molecular SRP-SR assembly and reports on the rate of conformational change.

***smFRET measurements.***

Labeled SRP-4A10L was diluted to 100-200 pM in SRP Assay Buffer. Unless otherwise specified, the samples contained 200 μM GppNHp, 150 nM 80S, and 1.5 μM SRαβΔTM where indicated. To measure conformational changes in SR, SR labeled with compaction probes was diluted to 100-200 pM in SRP Assay Buffer containing 200 μM GppNHp, 400 nM 80S, and 400 nM SRP or SRP-4A10L where indicated. With signal sequence and ribosome-bound SRP, these concentrations are sufficient to ensure that all labeled species are bound with the indicated binding

partners (*5*) (Fig. 5C). The samples were incubated at 25 °C for 5-10 minutes before measurements to ensure complete formation of the SRP•SR complex. Samples were placed in a closed chamber made by sandwiching a perforated silicone sheet (Grace Bio-Labs) with two coverslips to prevent potential evaporation during measurements. Data were collected over 30-60 min using an ALEX-FAMS setup with two single-photon Avalanche photodiodes (Perkin Elmer) and 532 nm (CNI laser) and 635 nm (Opto Engine LLC) continuous wave lasers operating at 150 μW and 70 μW, respectively (*32*, *33*).

All smFRET data analyses including burst search and burst selection were performed using FRETBursts (*34*), an open-source burst analysis toolkit for confocal smFRET. A dual-channel burst search (*69*) was performed to separate the particles containing FRET pairs from particles labeled with only the donor or acceptor dye. Each burst (assumed to be the fluorescence signal from an individual SRP or SR particle) was identified as a minimum of 10 consecutive detected photons with a photon count rate at between 6 to 15 times higher than the background photon count rate during both donor and acceptor excitation periods. Since the background rate can fluctuate within a measurement, the background rate was computed for every 50 second interval according to maximum likelihood fitting of the inter-photon delay distribution. The identified bursts were further selected according to the following criteria: (i) $n_{DD} + n_{DA} \geq 15$; and (ii) $n_{AA} \geq 15$, where $n_{DD}$ and $n_{DA}$ are the number of photons emitted from donor and acceptor during the donor excitation period, respectively, and $n_{AA}$ is the number of photons emitted from acceptor during the acceptor excitation period.

Under certain conditions, we observed some aggregated species that led to additional populations with different stoichiometry (S) values. The aggregated species are expected to show exceptionally long burst durations and/or multiple bursts that are close together if the dye

molecules undergo photo-physical events such as blinking. To filter out such aggregates, we first fused bursts that are less than 5 milliseconds apart, then removed bursts that have burst durations larger than 10 milliseconds. After applying this filter, the FRET populations showed a single Gaussian distribution in terms of S-value. In rare cases, aggregated species dominated the FRET population, and those data were discarded and not included in any of the analyses.

The uncorrected FRET efficiency (E*) and Stoichiometry (S) for each burst were calculated using the following equations:

$$E^* = \frac{n_{DA}}{n_{DD} + n_{DA}} \qquad (8)$$

$$S = \frac{n_{DD} + n_{DA}}{n_{DD} + n_{DA} + n_{AA}} \qquad (9)$$

FRET histograms were obtained by 1D projection of the 2D E*-S histograms onto the E* axis. In most cases, E* is different from actual FRET efficiency due to simplifying assumptions (*i.e. lk=0*, *dir=0*, *γ=1)*. However, since the correction factors only depend on the photo-physical properties of the fluorophores and the configuration of the optical setup, their contributions to FRET efficiency are constant as long as the same optical set up, FRET pair and labeling position are used throughout all measurements. Importantly, we did not observe any significant changes in the photo-physical properties of both the donor and acceptor dyes due to local environments (i.e. different conformations, substrates, ligands) (fig. S2). Therefore, conformational changes in SRP that alter the actual FRET efficiency will also change the E* value, and the trend of the changes with different binding partners will be the same.

For measurements with Proximal and Distal probes under each experimental condition, data from all replicates (n=2-9) were summed and were globally fit for each set of probes across the conditions. Fitting for each replicate experiment was also done with parameters from global

fitting, but the parameters were allowed to float for better fitting for each replicate. The Weighted Mean and SD of fitting parameters from individual fittings are shown in Table S2. Data from Compaction probes were not fit due to the dynamic nature of SR compaction.

***Burst Variance Analysis.***

Burst Variance Analysis (BVA) (*37*) was implemented to investigate conformational dynamics of SRP. Variance in fluorescence signal larger than the shot-noise limit can be attributed to static heterogeneity (i.e. mixture of stable multispecies with similar FRET values), dynamic heterogeneity (i.e. one species dynamically transitioning between states), or combination of dynamic and static heterogeneity. BVA can identify the dynamics of molecules by comparing the empirical standard deviation (SD) of E* of sub-bursts (containing fixed number of photons, *n*) within a burst to the expected shot-noise limited SD (i.e. Static limit). Eq. 10 was used to compute the static limit for a given mean E*.

$$\text{Static limit } (n, E^*) = \sqrt{\frac{E^*(1-E^*)}{n}} \qquad (10)$$

where $n = n_{DD} + n_{DA}$, the number of photons in a sub-burst. In this study, we used $n$ = 5. The static limits were represented as dashed curves in BVA plots (fig. S5**).** The observed SD ($\sigma_{E^*}$) for individual molecules was computed using Eq. 11.

$$\sigma_{E^*} = \sqrt{\frac{1}{M_i}\sum_{j=1}^{M_i}(e_{ij}^* - E_i^*)^2} \qquad (11)$$

where $M_i$ is the number of sub-bursts in the $i$ th burst, $e_{ij}^*$ is an uncorrected FRET efficiency of the $j$th sub-burst, and $E_i^*$ is the mean of all sub-bursts' uncorrected FRET efficiencies in the $i$ th burst. To reduce error that could arise from individual bursts, which only contain a small number of sub-bursts, we first binned bursts along the $E^*$ axis into 20 bins with a bin width of 0.05. All

of the sub-bursts in each bin within bursts were then used to calculate the observed SD for each bin ($SD_{E^*}$) using Eq. 12,

$$SD_{E^*} = \sqrt{\sum_{i \text{ where } L \le E_i^* < U} \sum_{j=1}^{M_i} \left[ \frac{(e_{ij}^* - \mu)^2}{\sum M_i} \right]} \qquad (12)$$

where $\mu = \sum_{i \text{ where } L \le E_i^* < U} \sum_{j=1}^{M_i} \left( e_{ij}^* \Big/ \sum M_i \right)$, $L$ is the lower bound of the bin, $\mu$ is the upper bound of the bin, $M_i$ is the number of sub-bursts in the $i$ th burst, and $e_{ij}^*$ is the uncorrected FRET efficiency of the $j$ th sub-burst in the $i$ th burst**.**

The dynamic score (DS) was computed using Eq. 13.

$$DS = \sqrt{\sum_{SD_{E^*} - SD_{E^*,\text{static}} > 0} (SD_{E^*} - SD_{E^*,\text{static}})^2} \qquad (13)$$

where $SD_{E^*,\text{static}}$ is the $SD_{E^*}$ of simulated static molecules using the Monte Carlo method and $N_{E^*}$ is the number of bursts in a given bin. The weighted dynamic score (WDS) was computed using Eq. 14 to take into account the different numbers of bursts in each bin.

$$WDS = \sqrt{\sum_{SD_{E^*} - SD_{E^*,\text{static}} > 0} \left( \frac{N_{E^*}}{\sum N_{E^*}} \right) (SD_{E^*} - SD_{E^*,\text{static}})^2} \qquad (14)$$

To ensure that the score reports on the dynamics of the major species in a given sample, only the $SD_{E^*}$ for bins with at least 5% of the total number of bursts in the entire FRET histogram (denoted by triangles in BVA plots in fig. S5**)** were used to calculate DS and WDS.

***Purification of complexes for cryoEM.***

Mammalian RNC harboring the signal sequence was prepared from rabbit reticulocyte system essentially as previously described (*19*). A DNA fragment containing sequences for the T7

promoter, Kozak, and a 3 ×FLAG tag, followed by LDKLIRVGIILVLLIWGTVLLLKSIPHHSNTPDYQEPNSNYTNDGKLKVSFSVVRNNTFHP KYHELH was cloned into EcoRI/PstI site of pUC57 plasmid (GenScript). The plasmid was linearized by PstI and then mRNA was generated by *in vitro* transcription using the T7 polymerase. The mRNA was then purified by LiCl precipitation followed by ethanol precipitation. The purified mRNA was translated in the Flexi® Rabbit Reticulocyte Lysate System (Promega) using an mRNA concentration of 214 ng/μL for 25 min at 32°C. For the purification of RNCs, 0.5 mL of ANTI-FLAG® M2 Affinity Gel (SIGMA-ALDRICH) equilibrated with buffer A (50 mM HEPES-KOH, pH 7.6, 100 mM KCl, 5 mM $MgCl_2$) was added to 4.7 mL of the translation reaction product and gently mixed for 2 h at 4°C. Following the removal of the lysate, the gel was washed by 10 mL of buffer B (50 mM HEPES-KOH, pH 7.6, 500 mM KCl, 5 mM $MgCl_2$) and then by 10 mL of buffer A. Then, RNCs were eluted in 3 x 1 mL of fractions of buffer A containing 0.1 mg/mL 3 × FLAG® Peptide (SIGMA-ALDRICH). The total eluate was pooled and was ultra-centrifuged using a TLA55 rotor (Beckman Coulter) at 50,000 rpm at 4 °C for 2 h, and the RNC pellet was resuspended into buffer C (50 mM HEPES-KOH, pH 7.6, 100 mM KOAc, 5 mM $Mg(OAc)_2$). The final concentration of RNC was 0.5–1 μM and stored at –80 °C.

***Data processing***

Contrast transfer function (CTF) was first calculated using GPU-accelerated computer program for accurate and robust real-time CTF (GCTF) (*70*) on electron dose weighted images. CTF was then carefully inspected for drift, and only images that extend beyond 5 Å were retained. A total of 1,295,211 particle-images were picked from the 18,762 dose-weighted frames, with RELION3 (*71*) using a Gaussian blob as a reference. After 25 iterations of two-dimensional (2D) image

classification in RELION3 on binned images (6.048 Å per pixel), a total of 976,456 particle-images were selected from the dataset, and further refined following the 3D-autorefine approach in RELION3 and using an empty 80S ribosome as a reference filtered to 60 Å resolution. Images were then subjected to 3D-focused classification without alignments by applying a circular mask onto the ribosome tunnel exit site.

The 3D classification of the particles yielded 8 classes; 4 classes were of empty ribosomes (no or partial SRP·SR density was observed) and two of which contained a density of the RNC·SRP complex and a small population for the prehandover SRP·SR state; these classes were not further processed. The remaining two classes contain EM-densities corresponding to the early A (124,604 particle images) and early B (114,838 particle images) states. To further improve the EM density of SRP·SR in the early A and B states, a second round of 3D classification was performed by focusing on the distal site of the SRP RNA, and the 3D class displaying the highest resolution features of SRP·SR were retained (32,936 and 29,742 particle images for early A and B, respectively). Finally, the selected particles from the two classes were refined separately at the full pixel size without binning (1.062 Å per pixel; box size is 448 × 448 pixels), resulting in an overall average reconstruction of 3.2 and 3.3 Å resolution for the RNC·SRP$_{G226E}$·SR early A and early B complexes, respectively. Local resolution and gold standard FSC plots using FSC = 0.143 as a criterion were calculated. Final post-processing of the maps was done in RELION3.

***Model building***

For the RNC·SRP$_{G226E}$·SR early A complex (fig. S6), coordinates of the rabbit 60S ribosomal subunit (PDB:3JAG) (*72*) and the SRP RNA Alu domain (PDB ID: 6FRK) were docked as rigid bodies into the cryo-EM maps and manually adjusted. All SRP proteins were mutated to the human

sequence. Coordinates of the SRP RNA, SRP68, and the SRX/β and the SRP54 NG and M domains at the proximal site were docked as separate 3 rigid bodies (SRP RNA proximal site including SRP54 M-domain, SRP RNA distal site including SRX/β and SRP68, and SRP54 NG domain) into the cryo-EM map. SR MoRF was modelled as a poly-alanine in COOT (Emsley and Cowtan, 2004). A model of early B state could be generated by docking the coordinates for SRP and SR from early A model as a rigid body; hence a separate model for early B state was not further refined. For model refinements, the resulting model of RNC·$SRP_{G226E}$·SR early A complex was then refined into the corresponding EM density and subjected to six cycles of real space refinements using phenix.real_space_refine in PHENIX (*73*), during which protein secondary structure, Ramachandran and side-chain rotamer restraints, RNA base-pair restraints were applied. The fit of the EM map was validated using the real space correlation coefficients (CCmask) between the model and the versus map Fourier Shell Correlation (FSC) at FSC = 0.5 as a cut-off criterion, which resulted in similar resolution as the half-set map FSC using FSC = 0.143 criterion. Images were prepared in either Chimera (*74*), ChimeraX (*75*) or PyMOL (*76*).

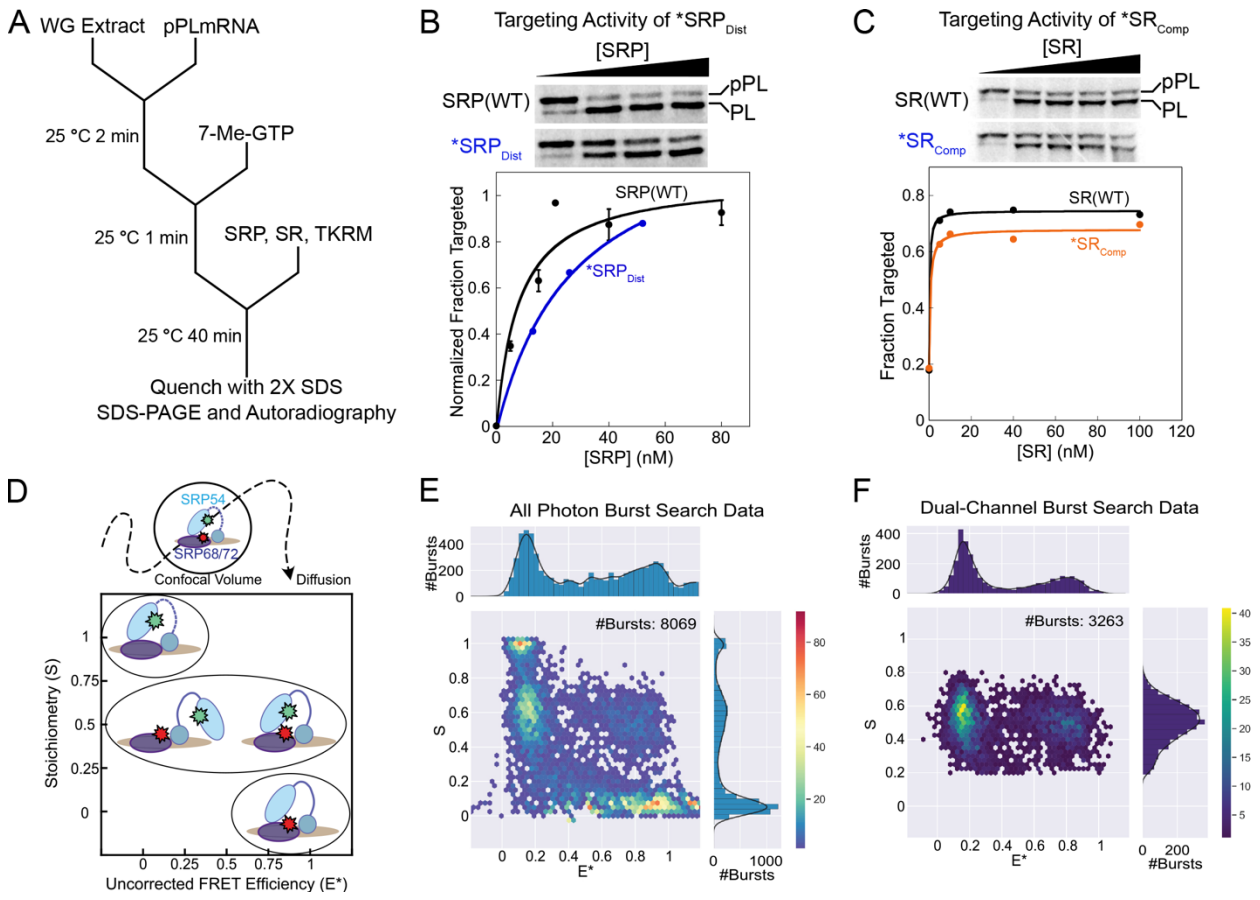


**Figure S1. Protein targeting and translocation activity of doubly-labeled SRP and SR, and experimental setup of the smFRET measurements.**

**(A)** Scheme to depict the *in vitro* protein targeting assay. Purified mRNA of a model SRP substrate, preprolactin (pPL), was translated in wheat germ lysate containing $^{35}$S-methionine. 1.5 mM 7-methyl-GTP was added 2 minutes after initiation of translation to inhibit additional rounds of translation. SRP, SR and high-salt washed, trypsin-digested rough ER microsomes (TKRM) were added to initiate the targeting reaction. The reactions were incubated at 25 °C for 40 min and quenched with SDS buffer, and analyzed by SDS-PAGE followed by autoradiography (*5*).

**(B)** Upper panel, representative SDS-PAGE autoradiography gels showing the translocation of pPL by wildtype SRP or $SRP_{Dist}$. Reactions contained 100 nM SR, indicated concentrations of SRP, and 0.5 eq of TKRM. Lower panel, quantification of pPL translocation efficiency from the data. The lower translocation with $SRP_{Dist}$ than SRP(WT) at lower SRP concentrations likely arose from a defect in RNC-$SRP_{Dist}$ binding, which was overcome at high SRP concentrations. For this reason, a large excess of RNC (200 nM) was used in all of the ALEX measurements with the $SRP_{Dis}$ probe, so that concentration-independent conformational changes are monitored.

**(C)** Upper panel, representative SDS-PAGE autoradiography gels showing the translocation of pPL by wildtype SR or $SR_{Comp}$. The reactions contained 20 nM SRP and 0.5 eq of TKRM. Lower panel, quantification of pPL translocation efficiency from the data.

**(D)** Scheme of the fluorescence-aided molecular sorting measurements using µs-ALEX. Fluorescently labeled SRPs diffusing through a femtoliter-scale confocal volume are alternately excited with donor and acceptor excitation lasers. The fluorescence from both donor (green) and acceptor (red) dyes are measured to calculate donor-acceptor stoichiometry (S) and uncorrected FRET efficiency (E*) to generate 2-D E*-S plots. This optically purifies the doubly labeled particles with both donor and acceptor dyes (S ~ 0.5), and 1D-projection of the doubly labeled population onto the E* axis generates the FRET histogram (*32–34*).

**(E, F)** Representative 2-D E*-S plots of $SRP_{Dist}$ bound with signal sequence, ribosome, and SR generated by all photon burst search (E) and dual-channel burst search (F). The dual-channel burst search filters out singly labeled species with only the donor (S ~1) or acceptor (S~0) dye.

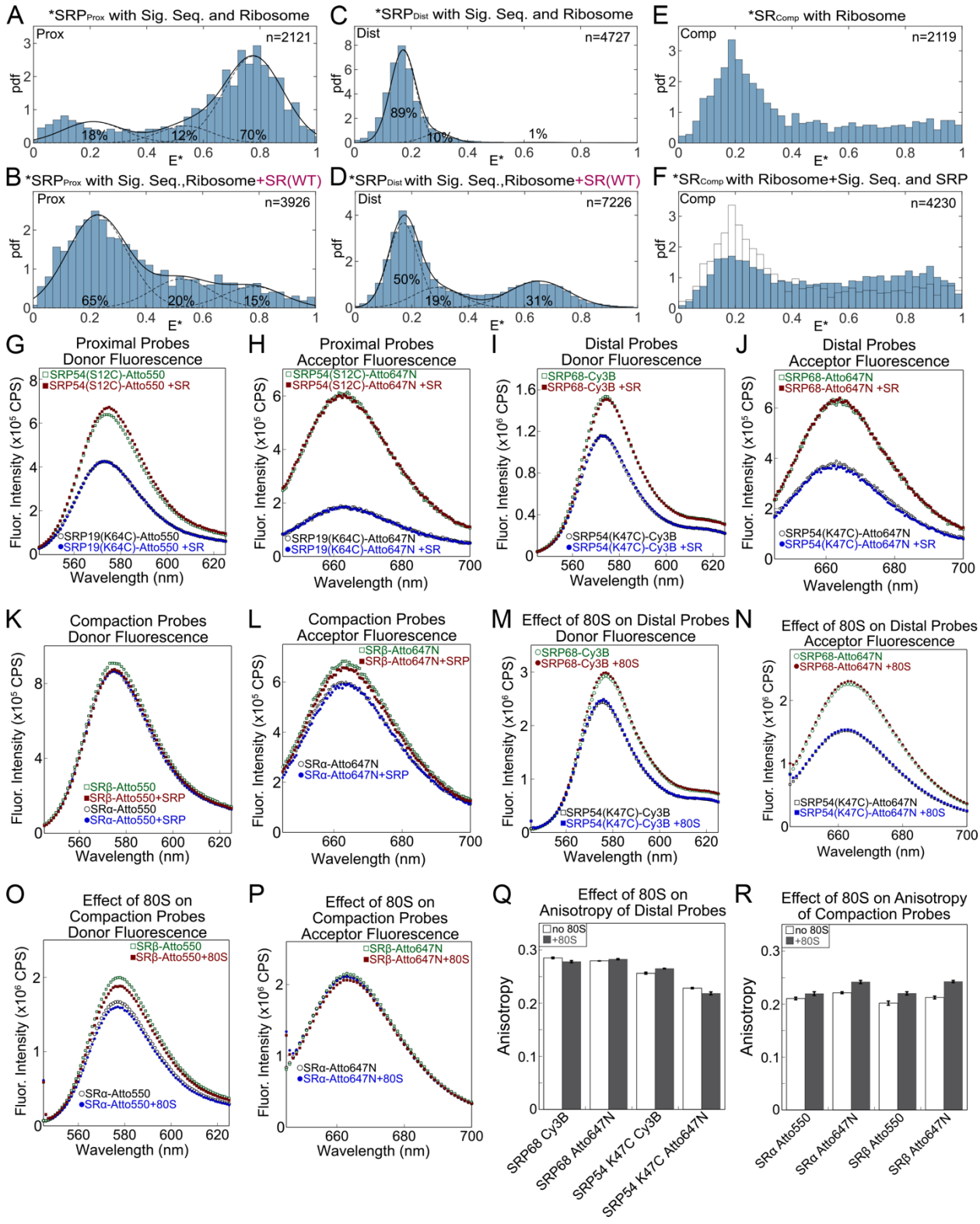


**Figure S2. The change in FRET efficiency is due only to the conformational change of the SRP.**

**(A-D)** FRET histograms of $SRP_{Prox}$ (A, B) and $SRP_{Dist}$ (C, D) in the absence (A, C) or presence (B, D) of SR, with the position of the donor and accepter dyes switched compared to those in Fig. 1.

**(E, F)** smFRET histograms of $SR_{Comp}$ bound to the ribosome with (F) and without (E) signal sequence-bound SRP present. The donor and acceptor dye positions were swapped compared to that in Fig. 1.

**(G-L)** Addition of SR or SRP did not affect the fluorescence intensity of the donor or acceptor dyes in $SRP_{Prox}$, $SRP_{Dist,}$ and $SR_{Comp}$. Steady-state fluorescence emission spectra are shown for SRP or SR singly labeled with the donor or acceptor dye at the indicated positions. Every labeling position was tested with both donor and acceptor dyes to exclude dye/position specific effects. The reactions contained the same concentrations of components as in the smFRET experiments, except that the labeled complexes were present at 15 nM.

**(M-P)** Addition of 80S did not affect the fluorescence intensity of the donor or acceptor dyes in $SRP_{Dist}$ and $SR_{Comp}$. Steady-state fluorescence emission spectra are shown for SRP or SR singly labeled with the donor or acceptor dyes at the indicated positions. The absence of an effect of 80S on the proximal probes have been reported previously (*5*).

**(Q, R)** Addition of 80S did not significantly affect the fluorescence anisotropy of the fluorescence dyes used for the Distal or Compaction probes. Fluorescence anisotropy was measured for the indicated fluorescence dyes labeled at the indicated positions in the absence and presence of 100 nM/400 nM 80S (for Distal/Compaction probes, respectively) to verify that the observed FRET changes are not due to dye orientational effects. Error bars represent SD, with n = 3.

A

| Mutation | Details |
|---|---|
| SRαΔX | Removed X/β |
| SR(Δ361) | Mutated SRα $^{361}$QLCESVAN to ALCAVVAA |
| SR(Δ371) | Replaced SRα 371-374 with $(GS)_2$ |
| SR(R407A) | Mutated SRα R407 to A |
| SR(Δ572) | Replaced SRα 572-581 with $(GS)_5$ |
| SRP54(G226E) | Mutated G226 to E in SRP54 |

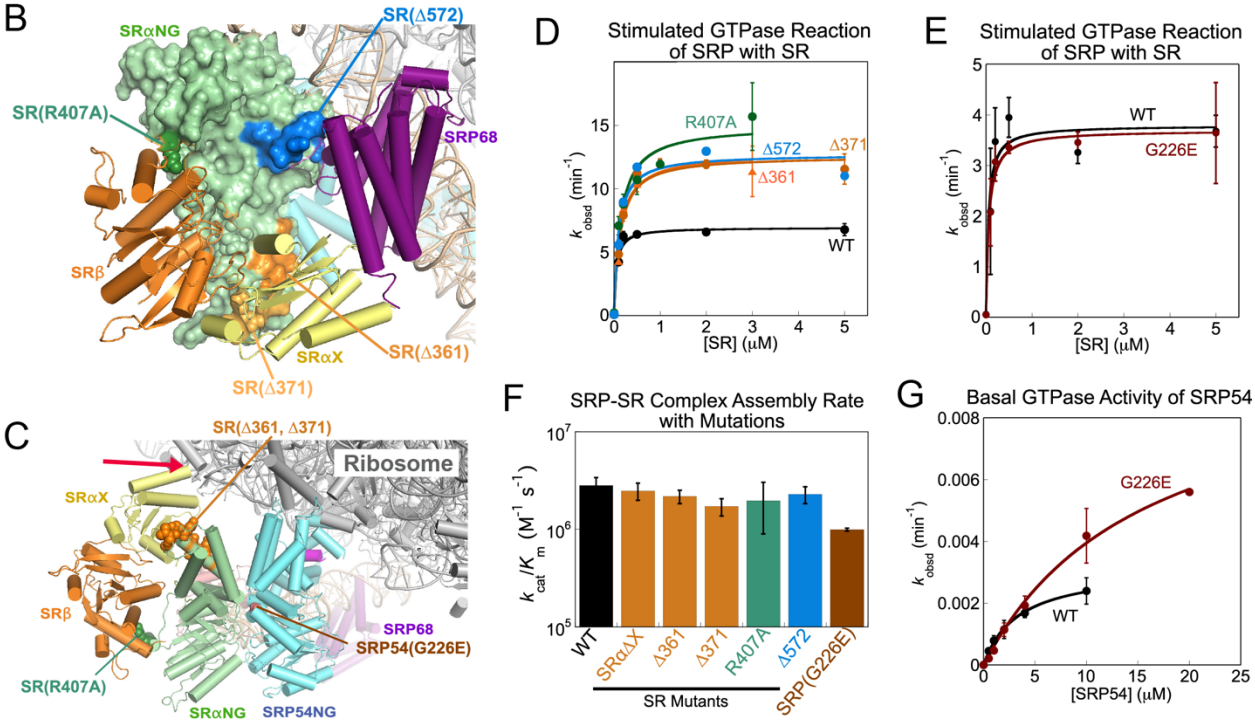


**Figure S3. Additional data for SRP and SR mutations that disrupt conformational changes in the targeting complex.**

**(A)** Details for the mutations characterized in this study.

**(B, C)** The location of the individual SRP and SR mutations are highlighted in the structure of the distal state complex (B; PDB: 6FRK) (*19*) and a structural model of the compacted SRP54-NG•SR complex at the ribosome exit site, generated by overlay of the SRP54-NG•SR complex in the distal state structure (PDB: 6FRK) (*19*) to SRP54-NG in the RNC•SRP complex (PDB: 3JAJ) (*16*). The red arrow indicates potential clash with the ribosome.

**(D)** The stimulated GTPase reaction between SRP and SR mutants. All reactions contained 0.2 μM SRP-4A10L,100 μM GTP, 0.25 μM 80S, and the indicated concentrations of wildtype or mutant SR. The lines are fits of the data to Eq. 2 and the obtained rate constants ($k_{cat}/K_m$ and $k_{cat}$) are summarized in panel (F) and Fig. 6A, respectively.

**(E)** The stimulated GTPase reaction between $SRP_{G226E}$ and SR. The reactions contained 0.2 μM SRP-4A10L or $SRP_{G226E}$-4A10L, 500 μM GTP, 0.25 μM 80S, and indicated concentrations of SR. The lines are fits of the data to Eq. 2 and the obtained rate constants ($k_{cat}/K_m$ and $k_{cat}$) are summarized in panel (F) and Fig. 6A, respectively.

**(F)** Summary of the values of $k_{cat}/K_m$ from parts (C) and (D).

**(G)** Basal GTPase reactions of wild-type SRP and $SRP_{G226E}$. Reactions were measured as described Supplementary Methods. The lines are fits of the data to Eq. 1 and gave rate constants of $k_{cat,wt} = 0.0032 \pm 0.00012$ $min^{-1}$, $K_{m,wt} = 3.3 \pm 0.29$ μM, $k_{cat,G226E} = 0.010 \pm 0.00087 min^{-1}$, and $K_{m,G226E} = 15.8 \pm 2.5$ μM.

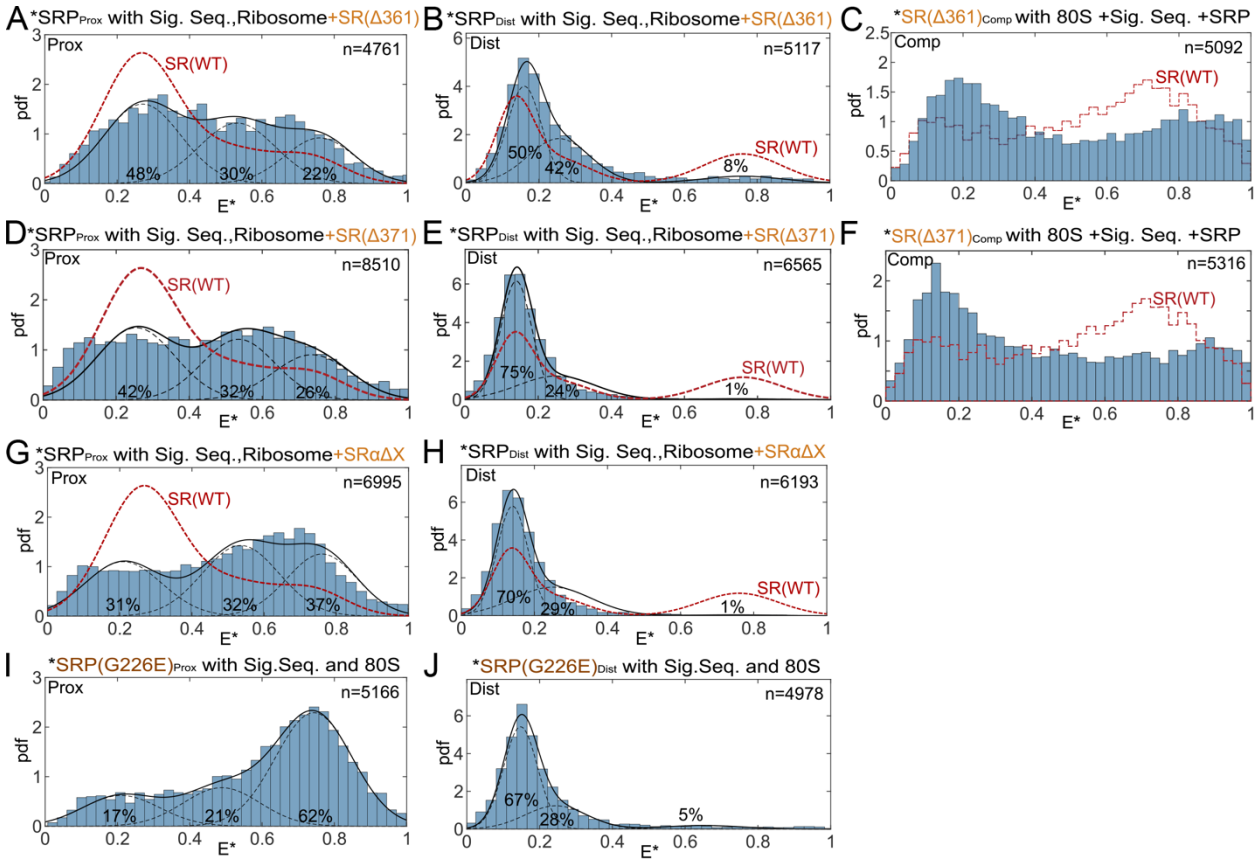


**Figure S4. The effect of SRP and SR mutations on the conformation of SRP and the SRP•SR complex.**

**(A-F)** smFRET histograms of the targeting complex assembled with SR(Δ361) (A-C) or SR(Δ371) (D-F), detected by the Proximal (A, D), Distal (B, E), and SR compaction (C, F) probes.

**(G, H)** smFRET histograms of the targeting complex assembled with SRαΔX, detected using the Proximal (G) and Distal (H) probes. The red lines in (A-H) outline the data with the wildtype targeting complex.

**(I, J)** smFRET histograms of ribosome- and signal-sequence bound SRP(G226E), detected using the proximal (I) or distal (J) probes.

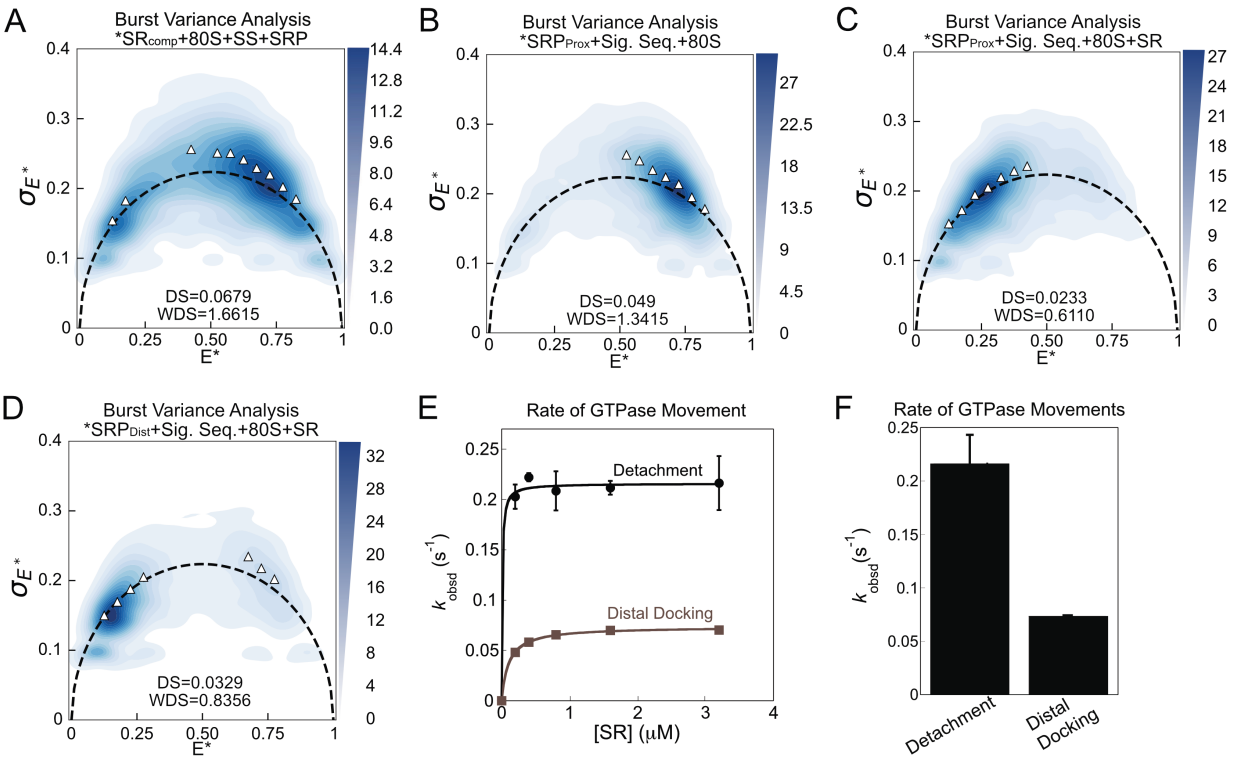


**Figure S5. Kinetic analysis supports a sequential model for the conformational rearrangements upon SRP-SR assembly.**

(**A**) Burst variance analysis of $SR_{Comp}$ in the targeting complex. The dashed curve depicts the static limit. Triangles denote the observed standard deviation for individual E* bins ($SD_{E^*}$) and were used to calculate the dynamic score (DS) and weighted dynamic score (WDS) (eqs 12-14 under Supplementary Methods).

**(B-D)** Burst variance analyses of signal sequence- and ribosome-bound $SRP_{Prox}$ (B), $SRP_{Prox}$ in the targeting complex (C), and $SRP_{Dist}$ in the targeting complex (D). The black dashed curve depicts the static limit. Triangles denote the observed standard deviation for individual E* bins ($SD_{E^*}$) and were used to calculate the dynamic score (DS) and weighted dynamic score (WDS) (eqs 12-14 in Supplementary Methods).

(**E**) The rate constants for movement of the SRP54-NG•SR complex from the ribosome exit site ('Detachment'), measured with SRP labeled with proximal probes, and for docking of this complex at the distal site ('Distal Docking') measured with the Distal probes. Changes in donor fluorescence intensity upon SR addition was monitored in real time on a stopped-flow apparatus to obtain the observed rate constants ($k_{obsd}$). Reactions contained 15 nM SRP-4A10L labeled with Proximal or Distal probes, 40 nM 80S, 200 μM GMPPNP, and the indicated SR concentrations. At saturating SR concentrations where $k_{obsd}$ is SR concentration-independent, $k_{obsd}$ is rate-limited by the unimolecular conformational change within the SRP•SR complex. Data are represented as mean ± SD, with n = 3-5.

(**F**) Summary of rate constants for detachment of the NG-complex from the ribosome exit (0.21 ± 0.027 $s^{-1}$) and for distal site docking (0.07 ± 0.0007 $s^{-1}$) from (E).

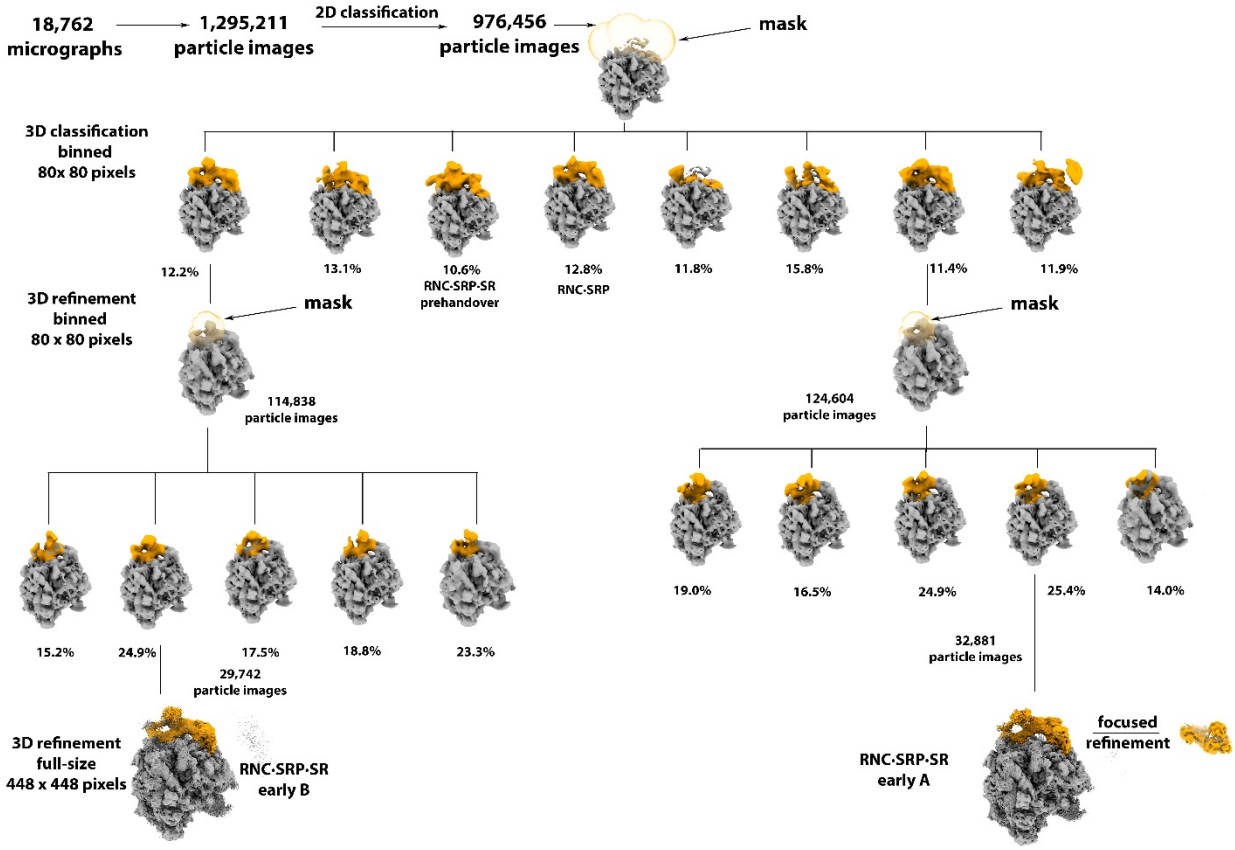


**Figure S6. Image classification and refinement of the structure of the RNC·SRP$_{G226E}$·SR.**

An initial 2D classification was performed on binned images with pixel size of 6.048 Å per pixel (box size 80 x 80 pixels) to remove bad particles. The selected particle images were then subjected to 3D refinement in RELION3 to obtain an initial map of the ribosome. Using binary mask applied at the ribosome tunnel region, a 3D focused classification without alignment was performed. This approach yielded a 3D class with a density corresponding RNC·SRP$_{G226E}$·SR, early A and B. A second round of focused 3D classification on binned images was performed for early A and early B classes which yielded two 3D classes with an improved EM density for SRP and SR at the distal site of the SRP RNA. The selected particle images in this 3D class were subjected to a 3D refinement using full size images without binning (448 x 448 pixels) in RELION3, which yielded a map with an overall resolution of 3.2 Å for both RNC·SRPG226E·SR early A and early B complexes. A focused refinement was performed on NG-domain on early A state to improve the density for MoRF.

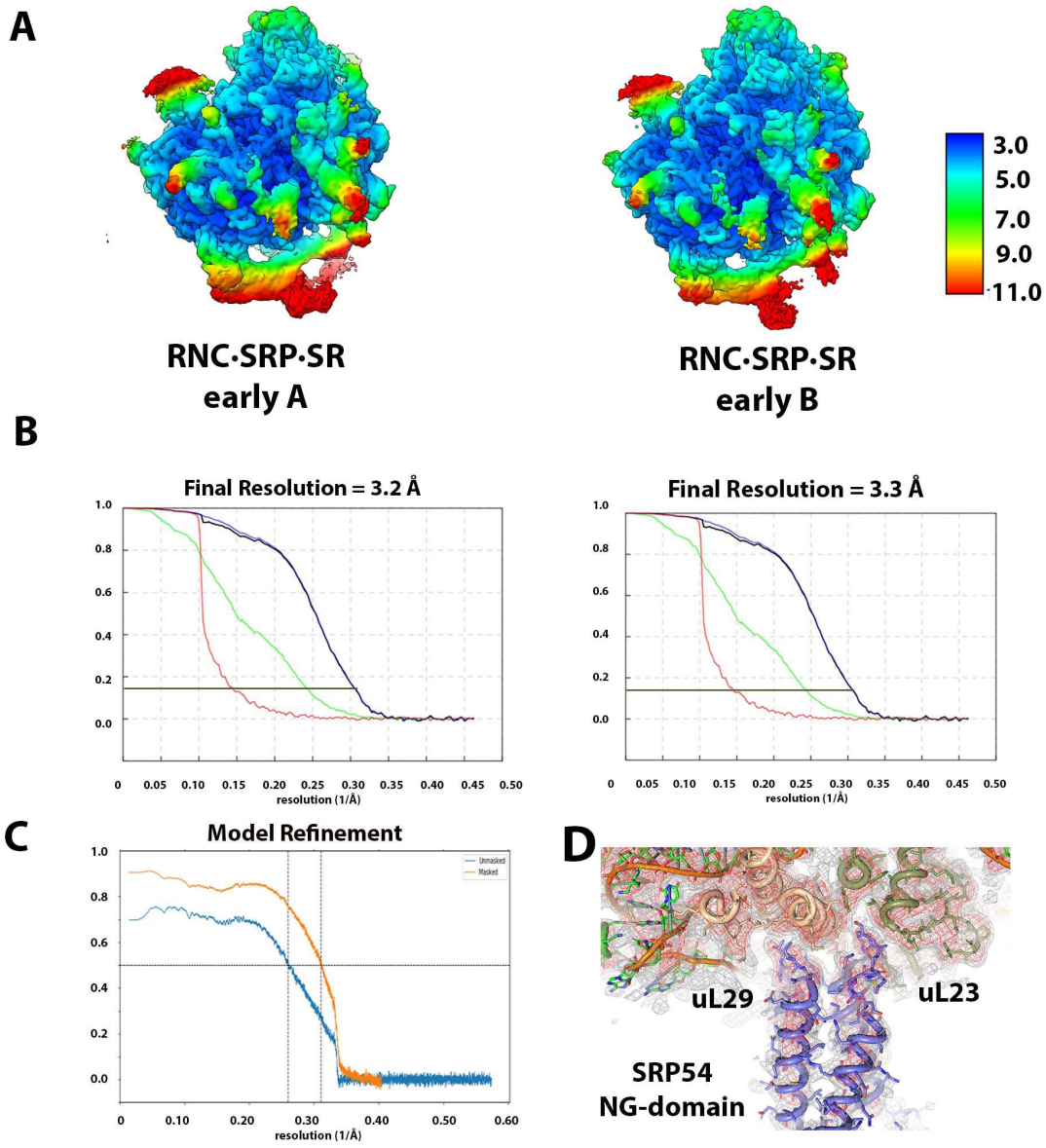


**Figure S7. Local resolution, Fourier Shell Correlation plots, and Model Validation.**

(**A**) Local resolution of RNC·SRP$_{G226E}$·SR early A (left), and early B (right) cryo-EM maps.

(**B**) Fourier Shell Correlation (FSC) plots for the cryo-EM maps, calculated using the gold standard FSC criteria cutoff (FSC=0.143) using independent two half maps as implemented in RELION3. The curves are of correlation-corrected (black), masked (blue), phase randomized (red) and unmasked (green) half-maps.

(**C**) Model versus map plots of RNC·SRP$_{G226E}$·SR early A complex. Resolution of the models is determined based on the FSC cutoff (FSC=0.5).

**(D)** Close-up view of the refined model RNC·$SRP_{G226E}$·SR early A model showing the SRP54 NG-domain (slate blue) contact sites with the ribosome at uL23 (olive) and uL29 (wheat).

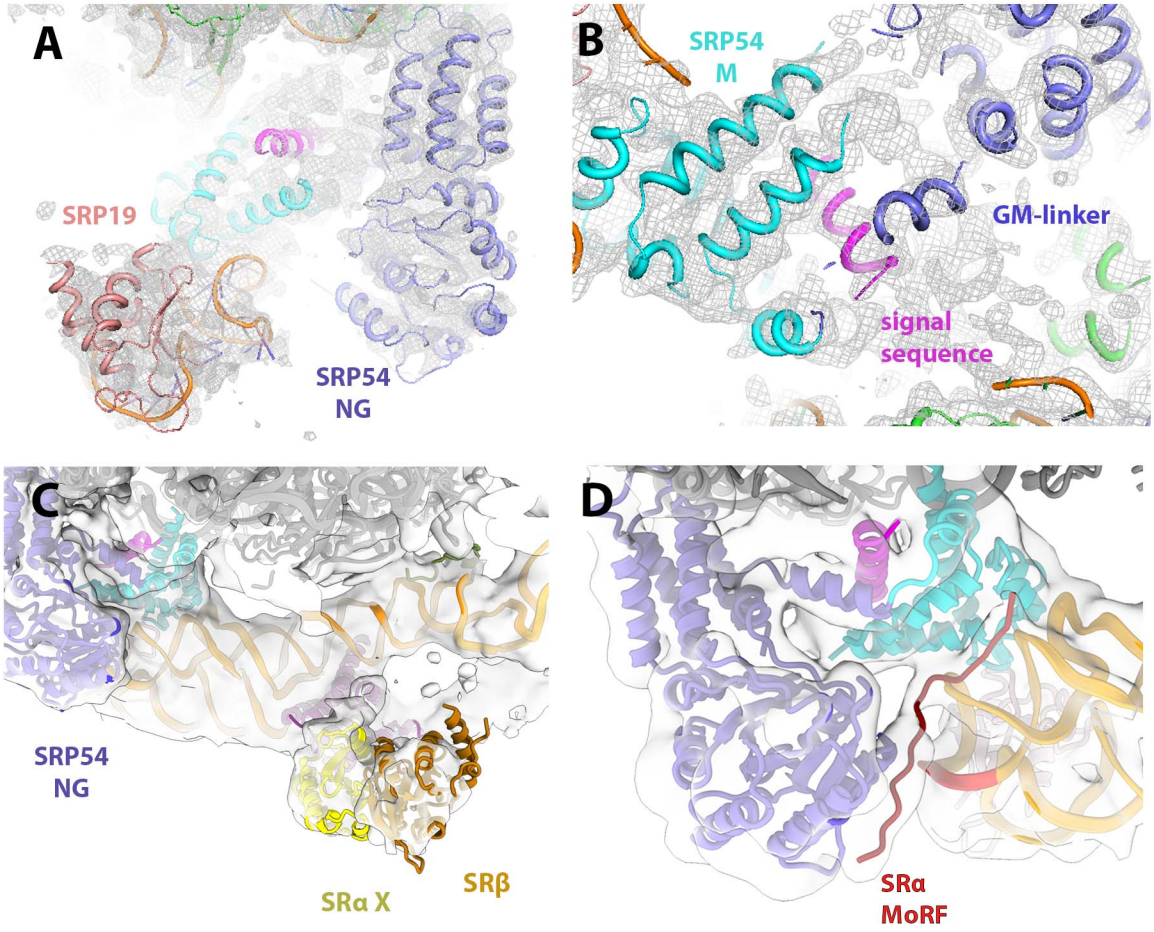


**Figure S8. Representative cryo-EM densities of the early A** RNC·**$SRP_{G226E}$·SR complex.**

(**A, B**) Close-ups of the SRP RNA proximal site depicting bound SRP54 NG-domain (slate blue) and SRP19 (salmon), and of the SRP54 M-domain (cyan) with bound signal sequence (magenta). Overlaid EM-density is shown as mesh and filtered to 4.5 Å resolution.

(**C, D**) Close-ups of the EM-density of the SRαX (yellow) and SRβ (brown) domains bound at the distal site of the SRP RNA (orange), and of the SRP RNA after focused 3D refinement depicting the density of the SRα MoRF (cherry) bound to SRP54 in close proximity of the SRP GNRA tetra-loop (red). Overlaid EM-density is shown as transparent surface and filtered to 8 Å resolution.

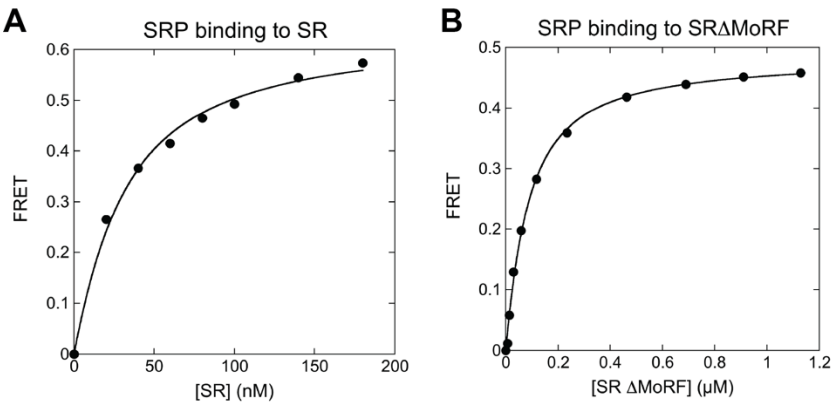


**Figure S9. Binding of SR and SRΔMoRF to SRP.**

The binding of SR **(A)** and SRΔMoRF **(B)** to wildtype SRP were measured using equilibrium titrations as described in Supplementary Methods. The data were fit to Eq 3, and the obtained $K_d$ values are summarized in Fig. 5C.

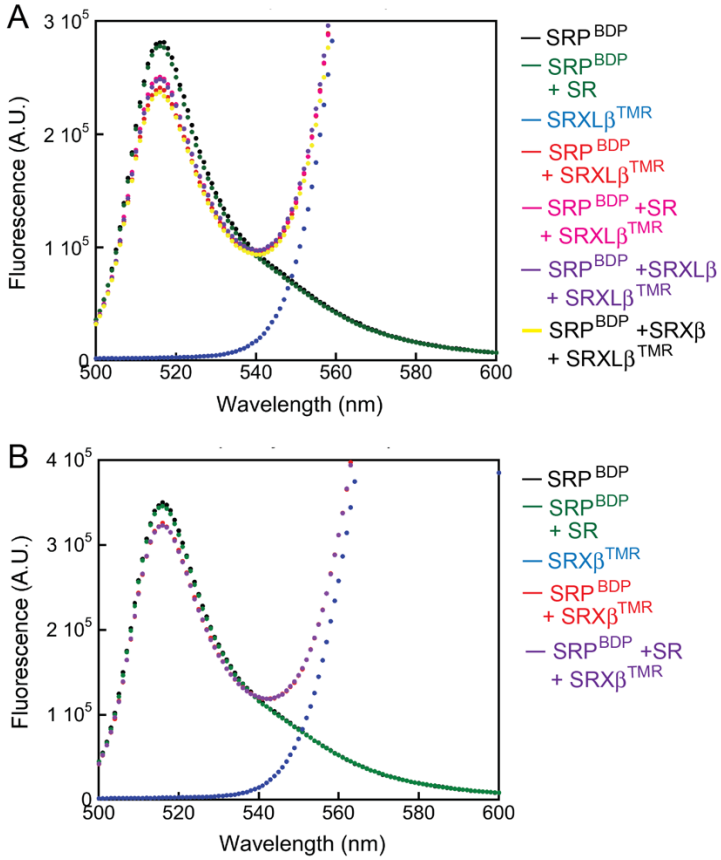


**Figure S10. FRET assay did not detect an interaction of SRXβ with SRP68.**

SRP was labeled with BODIPY-FL (BDP; donor dye) at SRP68(P149). SRXβ and SRXLβ were labeled with tetramethylrhodamine (TMR; acceptor dye) near the C-terminus of the X domain. The reactions contained 15 nM SRPBDP, 40 nM 80S, 2 μM $SRX\beta^{TMR}$ or $SRXL\beta^{TMR}$, and 10 μM unlabeled SR, SRXβ or SRXLβ where indicated. Fluorescence emission spectra were recorded using an excitation wavelength of 485 nm.

**(A)** Fluorescence emission spectra were recorded for the following samples: $SRP^{BDP}$ (donor only, black); $SRP^{BDP}$ with unlabeled SR (green); $SRXL\beta^{TMR}$ (acceptor only, blue); $SRP^{BDP}$ with $SRXL\beta^{TMR}$ (donor + acceptor, red); $SRP^{BDP}$ preincubated with unlabeled SR followed by addition of $SRXL\beta^{TMR}$ (magenta); $SRP^{BDP}$ preincubated with unlabeled SRXLβ followed by addition of $SRXL\beta^{TMR}$ (purple); $SRP^{BDP}$ preincubated with unlabeled SRXβ followed by addition of $SRXL\beta^{TMR}$ (yellow). Although 15% reduction in donor fluorescence intensity was observed (red line), this fluorescence change cannot be competed by a 5-fold excess of unlabeled SR constructs (magenta, purple, yellow), indicating that any interaction that generates the fluorescence change is not part of the wildtype SRP-SR complex.

**(B)** Fluorescence emission spectra were recorded for $SRP^{BDP}$ (donor only, black); $SRP^{BDP}$ with unlabeled SR (green); $SRX\beta^{TMR}$ (acceptor only, blue); $SRP^{BDP}$ with $SRX\beta^{TMR}$ (donor + acceptor, red); and $SRP^{BDP}$ preincubated with unlabeled SR followed by addition of $SRX\beta^{TMR}$ (purple).

Less than 5% reduction in donor fluorescence intensity was observed (red line), and this fluorescence change was competed by a 5-fold excess of unlabeled SR (purple), indicating that any interaction that generates the fluorescence change is not part of the wildtype SRP-SR complex.

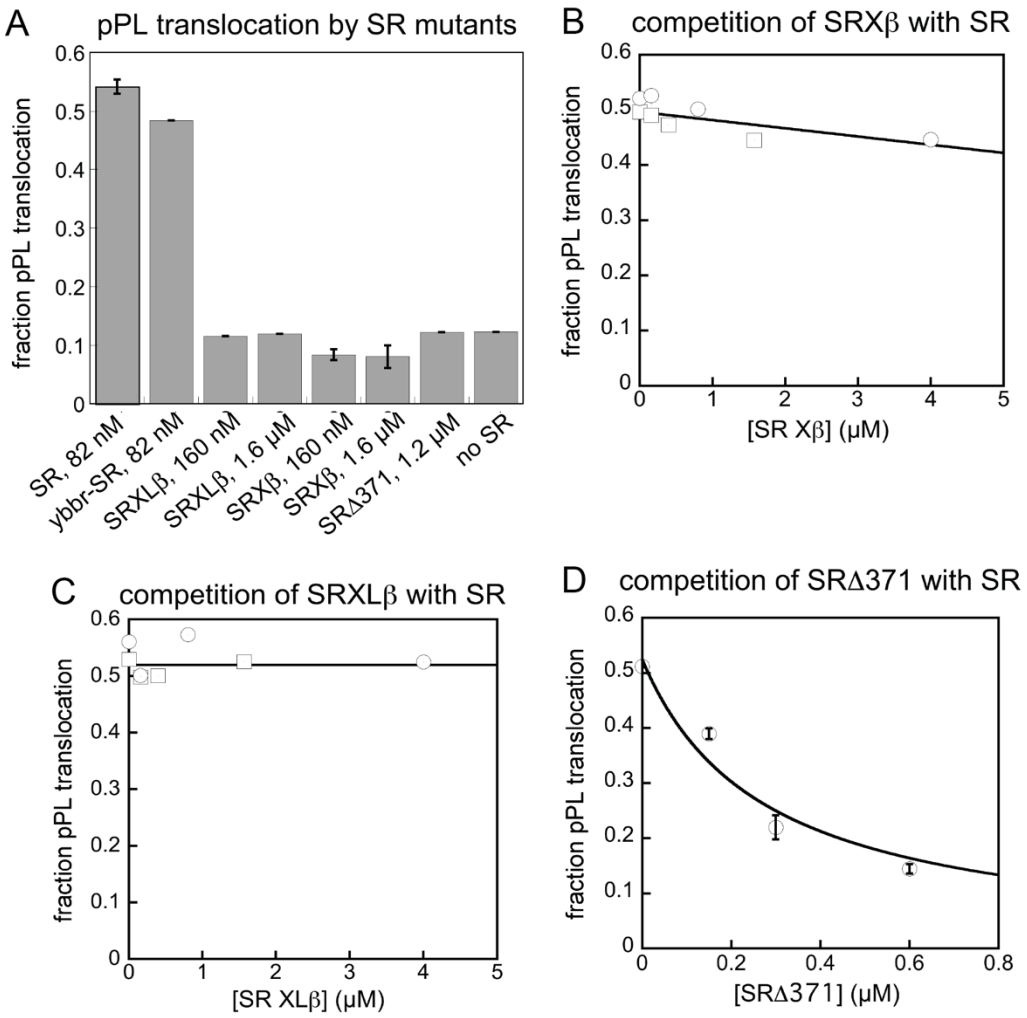


**Figure S11. SRXβ and SRXLβ do not effectively compete with wildtype SR during cotranslational protein translocation**.

(**A**) Cotranslational translocation of pPL were measured as in fig. S1, using 20 nM SRP and the indicated concentrations of SR variants. 'ybbr-SR' denotes SR with a ybbr at the C-terminus of the X-domain used for fluorescence labeling. Error bars denote SEM, with n = 2 biochemical replicates.

(**B, C**) A 40-fold excess of SRXβ (B) or SRXLβ (C) did not compete with SR and inhibit pPL translocation. Translocation reactions contained 20 nM SRP, 40 nM SR, and indicated concentrations of SRXβ or SRXLβ. Different symbols denote data from two independent biochemical measurements. Lines are linear fits to all the data points.

(**D**) As a control, sub-micromolar concentrations of SRΔ371 effectively competed with wildtype SR and inhibited translocation, consistent with the ability of this mutant to efficiently bind SRP (fig. S3, D and F). Translocation reactions contained 20 nM SRP, 40 nM SR, and the indicated concentrations of SRΔ371. As in the FRET measurements, SRΔ371 also contains the R458A

mutation that inhibits GTP hydrolysis of the SRP•SR complex and thus blocks dissociation of the complex following GTP hydrolysis.

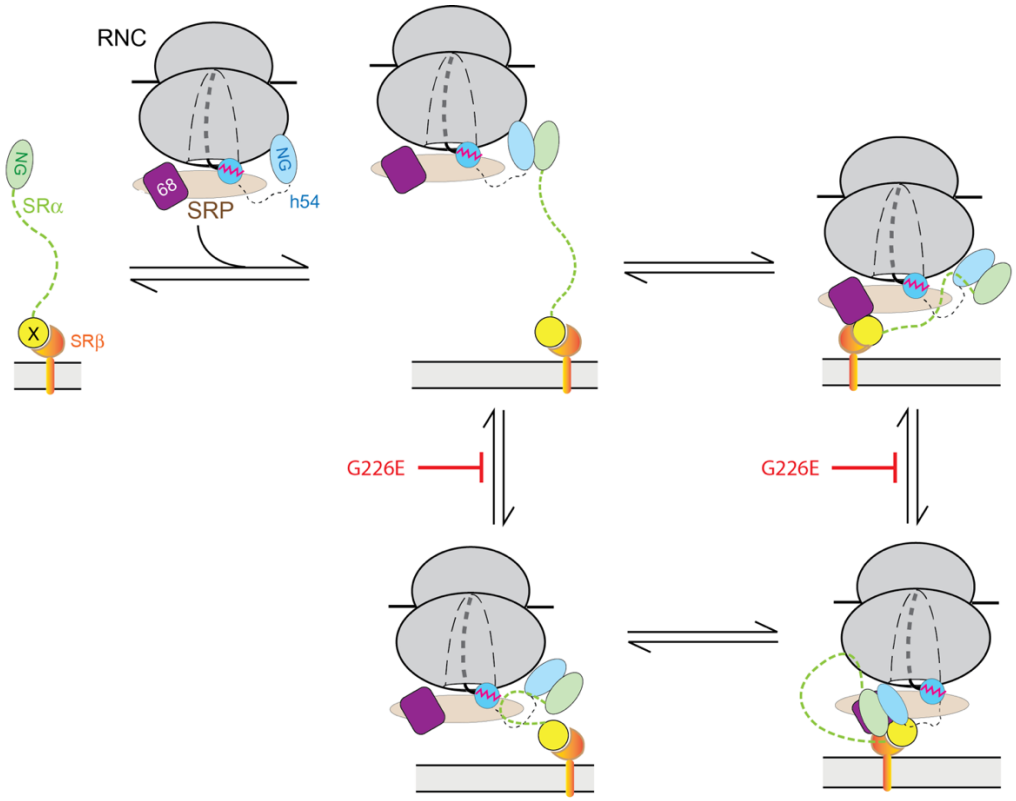


**Figure S12. Model for the effects of SRP(G226E) on the complex assembly pathway.** Two alternative pathways are shown for formation of the pre-handover complex. As SRP(G226E) blocks SR compaction, interaction of the SRXb domain with SRP68 is enabled by intramolecular chelate effects from interactions of the NG-domains and the SR MoRF.

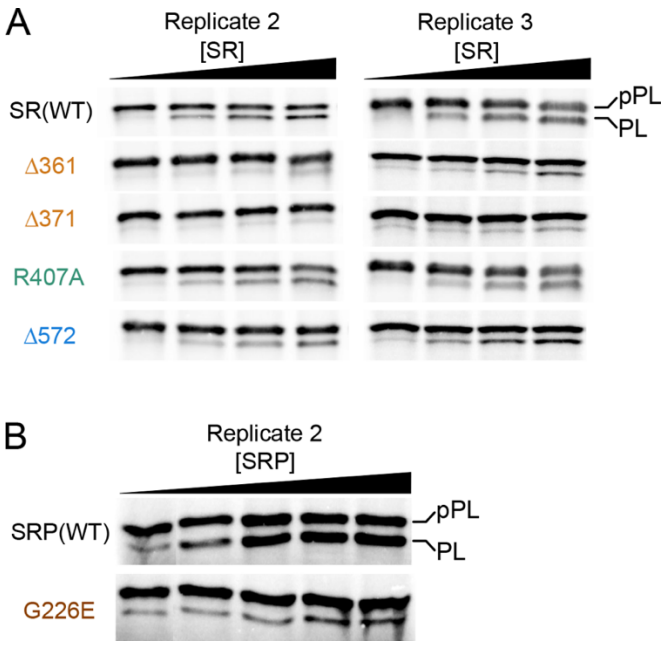


**Figure S13. SDS-PAGE autoradiographs for replicates of the translocation reactions mediated by the mutant SRP and SRs.**

Co-translational translocation of pPL mediated by wildtype or the indicated SR (**A**) and SRP (**B**) mutants. Replicate 1 and quantification of the translocation data are shown in Fig. 6.

| **Table S1. Cryo-EM data collection, map refinement, model refinement and validation statistics** | | |
|---|---|---|
| **Structure:** | early A intermediate | early B intermediate |
| EMDB accession / PDB code | 12303 / 7NFX | 12305 / - |
| **Data collection:** | | |
| Microscope | FEI Titan Krios | |
| Detector | Gatan K3 | |
| Voltage (keV) | 300 | |
| Electron exposure ($e^-/Å^2$) | 50 | |
| Pixel size (Å) | 1.062 | |
| Magnification (preGif) | 81,000x | |
| Defocus range (μm) | 1.5-2.5 | |
| Automation software | EPU | |
| **EM Reconstruction:** | | |
| Initial particle images (no.) | 1,295,211 | |
| Final particles (no.) | 32,881 | 29,697 |
| Resolution (unmasked / masked) at FSC=0.143 (Å) | 3.2 | 3.3 |
| Sharpening B-factor ($Å^2$) | -80.17 | -80.80 |
| **Coordinate real space refinement** | | |
| $CC_{mask}$ | 0.77 | |
| Resolution according to model vs. map FSC=0.143 / FSC=0.5 (masked) criterions (Å) | 3.21 / 3.41 | |
| Total atoms | 148,235 | |
| Protein residues | 7,693 | |
| RNA residues | 4,018 | |
| B factors ($Å^2$) | | |
| Protein | 9.04/138.21/ 38.23 | |
| RNA | 6.65/ 186.21/ 55.98 | |
| Ligand | 25.60/ 92.31/ 87.41 | |
| R.m.s. deviations | | |
| RMSD bonds (Å) | 0.002 | |
| RMSD angles (º) | 0.479 | |
| Validation | | |
| All-atom clashscore | 8.73 | |
| MolProbity score | 2.15 | |
| Ramachandran plot | | |

| | | |
|---|---|---|
| Favored (%) | 95.29 | |
| Allowed (%) | 4.63 | |
| Outliers (%) | 0.08 | |
| Rotamer outliers (%) | 2.89 | |

**Table S2. Summary of fitting parameters.**

Data are represented as weighted mean ± SD from at least three replicate measurements. Data without SD are SD=0 between replicate measurements. The data was fit globally for each set of probes to minimize variation of μ across conditions. Thus, our interpretations are mostly based on fraction in each FRET state, and small variations in μ are not meaningful.

| | | Fitting Parameters (μ(σ)) | | | Fraction | | |
|---|---|---|---|---|---|---|---|
| | **FRET state** | **Low** | **Median** | **High** | **Low** | **Median** | **High** |
| **Proximal Probes** | SRP Only | 0.26 (0.15) | 0.53 ± 0.0025 (0.12 ± 0.0092) | 0.74 ± 0.0028 (0.13 ± 0.0065) | 0.14 ± 0.019 | 0.18 ± 0.037 | 0.68 ± 0.043 |
| | SRP(G226E) | 0.30 (0.15) | 0.55 ± 0.0061 (0.11 ± 0.013) | 0.76 (0.14 ± 0.0032) | 0.23 ± 0.040 | 0.14 ± 0.019 | 0.64 ± 0.021 |
| | + SR (WT) | 0.26 ± 0.0041 (0.15 ± 0.0031) | 0.53 ± 0.0044 (0.15) | 0.74 ± 0.0042 (0.13 ± 0.0031) | 0.71 ± 0.034 | 0.18 ± 0.017 | 0.11 ± 0.019 |
| | + SRαΔX | 0.26 (0.15) | 0.54 (0.14 ± 0.0034) | 0.74 (0.14 ± 0.0089) | 0.31 ± 0.026 | 0.33 ± 0.0048 | 0.36 ± 0.025 |
| | + SR(R407A) | 0.26 ± 0.0015 (0.15) | 0.53 ± 0.0049 (0.15 ± 0.0070) | 0.74 ± 0.0042 (0.14 ± 0.0075) | 0.44 ± 0.054 | 0.30 ± 0.021 | 0.26 ± 0.048 |
| | + SR(Δ572) | 0.26 ± 0.0013 (0.15) | 0.53 ± 0.00084 (0.14 ± 0.014) | 0.74 ± 0.0029 (0.14 ± 0.012) | 0.67 ± 0.069 | 0.22 ± 0.045 | 0.10 ± 0.030 |
| | + SR(Δ371) | 0.26 (0.15) | 0.53 ± 0.0045 (0.14) | 0.74 ± 0.0045 (0.15) | 0.41 ± 0.0096 | 0.33 ± 0.0054 | 0.26 ± 0.0042 |
| | + SR(Δ361) | 0.30 (0.15) | 0.55 ± 0.0076 (0.14 ± 0.011) | 0.75 ± 0.0042 (0.14 ± 0.0091) | 0.48 ± 0.026 | 0.29 ± 0.052 | 0.23 ± 0.027 |
| **Distal Probes** | SRP Only | 0.14 (0.068 ± 0.0039) | 0.25 ± 0.00066 (0.092 ± 0.038) | 0.72 ± 0.038 (0.11 ± 0.062) | 0.88 ± 0.045 | 0.11 ± 0.039 | 0.013 ± 0.010 |
| | SRP(G226E) | 0.16 (0.062 ± 0.0033) | 0.25 (0.12) | 0.75 (0.15) | 0.67 ± 0.023 | 0.30 ± 0.025 | 0.033 ± 0.0023 |
| | + SR (WT) | 0.14 ± 0.00073 (0.070 ± 0.0050) | 0.25 ± 0.00025 (0.12 ± 0.028) | 0.75 ± 0.032 (0.15 ± 0.040) | 0.44 ± 0.053 | 0.22 ± 0.048 | 0.35 ± 0.029 |
| | + SRαΔX | 0.14 ± 0.00083 (0.065 ± 0.0021) | 0.25 (0.084 ± 0.015) | 0.72 ± 0.037 (0.13 ± 0.030) | 0.76 ± 0.061 | 0.22 ± 0.056 | 0.013 ± 0.0081 |
| | + SR(R407A) | 0.14 ± 0.00093 (0.065 ± 0.0044) | 0.25 ± 0.00092 (0.10 ± 0.015) | 0.72 ± 0.024 (0.15) | 0.73 ± 0.057 | 0.23 ± 0.054 | 0.041 ± 0.0072 |
| | + SR(Δ572) | 0.14 ± 0.0010 (0.070 ± 0.0071) | 0.25 ± 0.0010 (0.11 ± 0.011) | 0.71 ±0.014 (0.15) | 0.57 ± 0.047 | 0.33 ± 0.049 | 0.11 ± 0.013 |
| | + SR(Δ371) | 0.14 ± 0.00024 (0.065 ± 0.0037) | 0.25 (0.090 ± 0.012) | 0.70 (0.15) | 0.75 ± 0.037 | 0.24 ± 0.032 | 0.017 ± 0.0054 |
| | + SR(Δ361) | 0.17 ± 0.0056 (0.073 ± 0.0017) | 0.3 (0.09) | 0.75 (0.15) | 0.67 ± 0.043 | 0.25 ± 0.058 | 0.081 ± 0.015 |

## REFERENCES


1. F. U. Hartl, A. Bracher, M. Hayer-Hartl, Molecular chaperones in protein folding and proteostasis. *Nature* **475**, 324–332 (2011).

2. D. Akopian, K. Shen, X. Zhang, S. Shan, Signal recognition particle: An essential protein-targeting machine. *Annu. Rev. Biochem.* **82**, 693–721 (2013).

3. X. Zhang, S. Shan, Fidelity of cotranslational protein targeting by the signal recognition particle. *Annu. Rev. Biophys.* **43**, 381–408 (2014).

4. E. C. Mandon, Y. Jiang, R. Gilmore, Dual recognition of the ribosome and the signal recognition particle by the SRP receptor during protein targeting to the endoplasmic reticulum. *J. Cell Biol.* **162**, 575–585 (2003).

5. J. H. Lee, S. Chandrasekar, S. Chung, Y.-H. Hwang Fu, D. Liu, S. Weiss, S. Shan, Sequential activation of human signal recognition particle by the ribosome and signal sequence drives efficient protein targeting. *Proc. Natl. Acad. Sci. U.S.A.* **115**, E5487–E5496 (2018).

6. A. Jomaa, D. Boehringer, M. Leibundgut, N. Ban, Structures of the *E. coli* translating ribosome with SRP and its receptor and with the translocon. *Nat. Commun.* **7**, 10417 (2016).

7. K. Shen, X. Zhang, S.-o. Shan, Synergistic actions between the SRP RNA and translating ribosome allow efficient delivery of the correct cargos during cotranslational protein targeting. *RNA* **17**, 892–902 (2011).

8. X. Zhang, V. Q. Lam, Y. Mou, T. Kimura, J. Chung, S. Chandrasekar, J. R. Winkler, S. L. Mayo, S.-O. Shan, Direct visualization reveals dynamics of a transient intermediate during protein assembly. *Proc. Natl. Acad. Sci. U.S.A.* **108**, 6450–6455 (2011).

9. P. Walter, G. Blobel, [53] Signal recognition particle: A ribonucleoprotein required for cotranslational translocation of proteins, isolation and properties. *Methods Enzymol.* **96**, 682–691 (1983).

10. S. Angelini, D. Boy, E. Schiltz, H.-G. Koch, Membrane binding of the bacterial signal recognition particle receptor involves two distinct binding sites. *J. Cell Biol.* **174**, 715–724 (2006).

11. E. de Leeuw, K. te Kaat, C. Moser, G. Menestrina, R. Demel, B. de Kruijff, B. Oudega, J. Luirink, I. Sinning, Anionic phospholipids are involved in membrane association of FtsY and stimulate its GTPase activity. *EMBO J.* **19**, 531–541 (2000).

12. S. Tajima, L. Lauffer, V. L. Rath, P. Walter, The signal recognition particle receptor is a complex that contains two distinct polypeptide chains. *J. Cell Biol.* **103**, 1167–1178 (1986).

13. T. Schwartz, G. Blobel, Structural basis for the function of the β subunit of the eukaryotic signal recognition particle receptor. *Cell* **112**, 793–803 (2003).

14. Y.-H. Hwang Fu, S. Chandrasekar, J. H. Lee, S. Shan, A molecular recognition feature mediates ribosome-induced SRP-receptor assembly during protein targeting. *J. Cell Biol.* **218**, 3307–3319 (2019).

15. L. F. Estrozi, D. Boehringer, S. Shan, N. Ban, C. Schaffitzel, Cryo-EM structure of the *E. coli* translating ribosome in complex with SRP and its receptor. *Nat. Struct. Mol. Biol.* **18**, 88–90 (2011).

16. R. M. Voorhees, R. S. Hegde, Structures of the scanning and engaged states of the mammalian SRP-ribosome complex. *eLife* **4**, e07975 (2015).

17. M. Halic, T. Becker, M. R. Pool, C. M. T. Spahn, R. A. Grassucci, J. Frank, R. Beckmann, Structure of the signal recognition particle interacting with the elongation-arrested ribosome. *Nature* **427**, 808–814 (2004).

18. M. Halic, M. Gartmann, O. Schlenker, T. Mielke, M. R. Pool, I. Sinning, R. Beckmann, Signal recognition particle receptor exposes the ribosomal translocon binding site. *Science* **312**, 745–747 (2006).

19. K. Kobayashi, A. Jomaa, J. H. Lee, S. Chandrasekar, D. Boehringer, S. Shan, N. Ban, Structure of a prehandover mammalian ribosomal SRP·SRP receptor targeting complex. *Science* **360**, 323–327 (2018).

20. B. Jadhav, M. McKenna, N. Johnson, S. High, I. Sinning, M. R. Pool, Mammalian SRP receptor switches the Sec61 translocase from Sec62 to SRP-dependent translocation. *Nat. Commun.* **6**, 10133 (2015).

21. T. Connolly, P. Rapiejko, R. Gilmore, Requirement of GTP hydrolysis for dissociation of the signal recognition particle from its receptor. *Science* **252**, 1171–1173 (1991).

22. P. J. Rapiejko, R. Gilmore, Empty site forms of the SRP54 and SRα GTPases mediate targeting of ribosome-nascent chain complexes to the endoplasmic reticulum. *Cell* **89**, 703–713 (1997).

23. C. Wilson, T. Connolly, T. Morrison, R. Gilmore, Integration of membrane proteins into the endoplasmic reticulum requires GTP. *J. Cell Biol.* **107**, 69–77 (1988).

24. P. J. Chitwood, S. Juszkiewicz, A. Guna, S. Shao, R. S. Hegde, EMC is required to initiate accurate membrane protein topogenesis. *Cell* **175**, 1507–1519.e16 (2018).

25. M. J. Shurtleff, D. N. Itzhak, J. A. Hussmann, N. T. Schirle Oakdale, E. A. Costa, M. Jonikas, J. Weibezahn, K. D. Popova, C. H. Jan, P. Sinitcyn, S. S. Vembar, H. Hernandez, J. Cox, A. L. Burlingame, J. L. Brodsky, A. Frost, G. H. Borner, J. S. Weissma, The ER membrane protein complex interacts cotranslationally to enable biogenesis of multipass membrane proteins. *eLife* **7**, e37018 (2018).

26. G. J. Phillips, T. J. Silhavy, The *E. coli* ffh gene is necessary for viability and efficient protein export. *Nature* **359**, 744–746 (1992).

27. S. M. Althoff, S. W. Stevens, J. A. Wise, The Srp54 GTPase is essential for protein export in the fission yeast Schizosaccharomyces pombe. *Mol. Cell. Biol.* **14**, 7839–7854 (1994).

28. C. Schürch, T. Schaefer, J. S. Müller, P. Hanns, M. Arnone, A. Dumlin, J. Schärer, I. Sinning, K. Wild, J. Skokowa, K. Welte, R. Carapito, S. Bahram, M. Konantz, C. Lengerke, SRP54 mutations induce Congenital Neutropenia via dominant-negative effects on XBP1 splicing. *Blood* **137**, 1340–1352 (2021).

29. R. Carapito, M. Konantz, C. Paillard, Z. Miao, A. Pichot, M. S. Leduc, Y. Yang, K. L. Bergstrom, D. H. Mahoney, D. L. Shardy, G. Alsaleh, L. Naegely, A. Kolmer, N. Paul, A. Hanauer, V. Rolli, J. S. Müller, E. Alghisi, L. Sauteur, C. Macquin, A. Morlon, C. S. Sancho, P. Amati-Bonneau, V. Procaccio, A.-L. Mosca-Boidron, N. Marle, N. Osmani, O. Lefebvre, J. G. Goetz, S. Unal, N. A. Akarsu, M. Radosavljevic, M.-P. Chenard, F. Rialland, A. Grain, M.-C. Béné, M. Eveillard, M. Vincent, J. Guy, L. Faivre, C. Thauvin-Robinet, J. Thevenon, K. Myers, M. D. Fleming, A. Shimamura, E. Bottollier-Lemallaz, E. Westhof, C. Lengerke, B. Isidor, S. Bahram, Mutations in signal recognition particle SRP54 cause syndromic neutropenia with Shwachman-Diamond–like features. *J. Clin. Invest.* **127**, 4090–4103 (2017).

30. C. Bellanné-Chantelot, B. Schmaltz-Panneau, C. Marty, O. Fenneteau, I. Callebaut, S. Clauin, A. Docet, G. L. Damaj, T. Leblanc, I. Pellier, C. Stoven, S. Souquere, I. Antony-Debré, B. Beaupain, N. Aladjidi, V. Barlogis, F. Bauduer, P. Bensaid, O. Boespflug-Tanguy, C. Berger, Y. Bertrand, L. Carausu, C. Fieschi, C. Galambrun, A. Schmidt, H. Journel, F. Mazingue, B. Nelken, T. C. Quah, E. Oksenhendler, M. Ouachée, M. Pasquet, V. Saada, F. Suarez, G. Pierron, W. Vainchenker, I. Plo, J. Donadieu, Mutations in the SRP54 gene cause severe congenital neutropenia as well as Shwachman-Diamond – Like syndrome. *Blood* **132**, 1318–1331 (2018).

31. K. D. Juaire, K. Lapouge, M. M. M. Becker, I. Kotova, M. Michelhans, R. Carapito, K. Wild, S. Bahram, I. Sinning, Structural and functional impact of SRP54 mutations causing severe congenital neutropenia. *Structure* **29**, 15–28.e7 (2021).

32. A. N. Kapanidis, N. K. Lee, T. A. Laurence, S. Doose, E. Margeat, S. Weiss, Fluorescence-aided molecule sorting: Analysis of structure and interactions by alternating-laser excitation of single molecules. *Proc. Natl. Acad. Sci. U.S.A.* **101**, 8936–8941 (2004).

33. A. N. Kapanidis, T. A. Laurence, N. K. Lee, E. Margeat, X. Kong, S. Weiss, Alternating-laser excitation of single molecules. *Acc. Chem. Res.* **38**, 523–533 (2005).

34. A. Ingargiola, E. Lerner, S. Chung, S. Weiss, X. Michalet, FRETBursts: An open source toolkit for analysis of freely-diffusing single-molecule FRET. *PLOS ONE* **11**, e0160716 (2016).

35. S. C. Ogg, W. P. Barz, P. Walter, A FUnctional GTPase domain, but not its transmembrane domain, is required for function of the SRP receptor β-subunit. *J. Cell Biol.* **142**, 341–354 (1998).

36. T. A. Fulga, I. Sinning, B. Dobberstein, M. R. Pool, SRβ coordinates signal sequence release from SRP with ribosome binding to the translocon. *EMBO J.* **20**, 2338–47 (2001).

37. J. P. Torella, S. J. Holden, Y. Santoso, J. Hohlbein, A. N. Kapanidis, Identifying molecular dynamics in single-molecule FRET experiments with burst variance analysis. *Biophys. J.* **100**, 1568–1577 (2011).

38. N. C. Robb, T. Cordes, L. C. Hwang, K. Gryte, D. Duchi, T. D. Craggs, Y. Santoso, S. Weiss, R. H. Ebright, A. N. Kapanidis, The transcription bubble of the RNA polymerase-promoter open complex exhibits conformational heterogeneity and millisecond-scale dynamics: Implications for transcription start-site selection. *J. Mol. Biol.* **425**, 875–885 (2013).

39. U. S. Chio, S. Chung, S. Weiss, S. Shan, A protean clamp guides membrane targeting of tail-anchored proteins. *Proc. Natl. Acad. Sci.* **114**, E8585–E8594 (2017).

40. H.-H. Hsieh, J. H. Lee, S. Chandrasekar, S. Shan, A ribosome-associated chaperone enables substrate triage in a cotranslational protein targeting complex. *Nat. Commun.* **11**, 5840 (2020).

41. K. Shen, Y. Wang, Y.-H. Hwang Fu, Q. Zhang, J. Feigon, S. Shan, Molecular mechanism of GTPase activation at the signal recognition particle (SRP) RNA distal end. *J. Biol. Chem.* **288**, 36385–36397 (2013).

42. F. Voigts-Hoffmann, N. Schmitz, K. Shen, S. Shan, S. F. Ataide, N. Ban, The structural basis of FtsY recruitment and GTPase activation by SRP RNA. *Mol. Cell* **52**, 643–654 (2013).

43. S. Shan, S. Chandrasekar, P. Walter, Conformational changes in the GTPase modules of the signal reception particle and its receptor drive initiation of protein translocation. *J. Cell Biol.* **178**, 611–620 (2007).

44. X. Zhang, R. Rashid, K. Wang, S.-o. Shan, Sequential checkpoints govern substrate selection during cotranslational protein targeting. *Science* **328**, 757–760 (2010).

45. S. Light, R. Sagit, O. Sachenkova, D. Ekman, A. Elofsson, Protein expansion is primarily due to indels in intrinsically disordered regions. *Mol. Biol. Evol.* **30**, 2645–2653 (2013).

46. R. Parlitz, A. Eitan, G. Stjepanovic, L. Bahari, G. Bange, E. Bibi, I. Sinning, *Escherichia coli* signal recognition particle receptor FtsY contains an essential and autonomous membrane-binding amphipathic helix. *J. Biol. Chem.* **282**, 32176–32184 (2007).

47. V. Q. Lam, D. Akopian, M. Rome, D. Henningsen, S. Shan, Lipid activation of the signal recognition particle receptor provides spatial coordination of protein targeting. *J. Cell Biol.* **190**, 623–635 (2010).

48. Y. Nyathi, B. M. Wilkinson, M. R. Pool, Co-translational targeting and translocation of proteins to the endoplasmic reticulum. *Biochim. Biophys. Acta Mol. Cell Res.* **1833**, 2392–2402 (2013).

49. S. Shan, R. M. Stroud, P. Walter, Mechanism of association and reciprocal activation of two GTPases. *PLOS Biol.* **2**, e320 (2004).

50. P. F. Egea, S. O. Shan, J. Napetschnig, D. F. Savage, P. Walter, R. M. Stroud, Substrate twinning activates the signal recognition particle and its receptor. *Nature* **427**, 215–221 (2004).

51. P. J. Focia, I. V. Shepotinovskaya, J. A. Seidler, D. M. Freymann, Heterodimeric GTPase core of the SRP targeting complex. *Science* **303**, 373–377 (2004).

52. K. Wild, G. Bange, D. Motiejunas, J. Kribelbauer, A. Hendricks, B. Segnitz, R. C. Wade, I. Sinning, Structural basis for conserved regulation and adaptation of the signal recognition particle targeting complex. *J. Mol. Biol.* **428**, 2880–2897 (2016).

53. S. Kanda, K. Yanagitani, Y. Yokota, Y. Esaki, K. Kohno, Autonomous translational pausing is required for XBP1u mRNA recruitment to the ER via the SRP pathway. *Proc. Natl. Acad. Sci.* **113**, E5886–E5895 (2016).

54. G. E. Karagöz, D. Acosta-Alvear, P. Walter, The unfolded protein response: Detecting and responding to fluctuations in the protein-folding capacity of the endoplasmic reticulum. *Cold Spring Harb. Perspect. Biol.* **11**, a033886 (2019).

55. K. Shen, S. Arslan, D. Akopian, T. Ha, S. Shan, Activated GTPase movement on an RNA scaffold drives co-translational protein targeting. *Nature* **492**, 271–275 (2012).

56. A. Jomaa, Y.-H. H. Fu, D. Boehringer, M. Leibundgut, S. Shan, N. Ban, Structure of the quaternary complex between SRP, SR, and translocon bound to the translating ribosome. *Nat. Commun.* **8**, 15470 (2017).

57. P. Walter, G. Blobel, Subcellular distribution of signal recognition particle and 7SL-RNA determined with polypeptide-specific antibodies and complementary DNA probe. *J. Cell Biol.* **97**, 1693–1699 (1983).

58. I. Yosef, E. S. Bochkareva, J. Adler, E. Bibi, Membrane protein biogenesis in Ffh- or FtsY-depleted *Escherichia coli*. *PLOS ONE* **5**, e9130 (2010).

59. Y. Ishihama, T. Schmidt, J. Rappsilber, M. Mann, F. U. Hartl, M. J. Kerner, D. Frishman, Protein abundance profiling of the *Escherichia coli* cytosol. *BMC Genomics* **9**, 102 (2008).

60. Z. Cheng, R. Gilmore, Slow translocon gating causes cytosolic exposure of transmembrane and lumenal domains during membrane protein integration. *Nat. Struct. Mol. Biol.* **13**, 930–936 (2006).

61. N. Aviram, M. Schuldiner, Targeting and translocation of proteins to the endoplasmic reticulum at a glance. *J. Cell Sci.* **130**, 4079–4085 (2017).

62. P. J. Chitwood, R. S. Hegde, The role of EMC during membrane protein biogenesis. *Trends Cell Biol.* **29**, 371–384 (2019).

63. K. Yanagitani, Y. Imagawa, T. Iwawaki, A. Hosoda, M. Saito, Y. Kimata, K. Kohno, Cotranslational targeting of XBP1 protein to the membrane promotes cytoplasmic splicing of its own mRNA. *Mol. Cell* **34**, 191–200 (2009).

64. K. Yanagitani, Y. Kimata, H. Kadokura, K. Kohno, Translational pausing ensures membrane targeting and cytoplasmic splicing of XBP1u mRNA. *Science* **331**, 586–589 (2011).

65. J. Yin, A. J. Lin, D. E. Golan, C. T. Walsh, Site-specific protein labeling by Sfp phosphopantetheinyl transferase. *Nat. Protoc.* **1**, 280–285 (2006).

66. P. Peluso, S. Shan, S. Nock, D. Herschlag, P. Walter, Role of SRP RNA in the GTPase cycles of Ffh and FtsY. *Biochemistry* **40**, 15224–15233 (2001).

67. S. Q. Zheng, E. Palovcak, J.-P. Armache, K. A. Verba, Y. Cheng, D. A. Agard, MotionCor2: Anisotropic correction of beam-induced motion for improved cryo-electron microscopy. *Nat. Methods* **14**, 331–332 (2017).

68. R. Gilmore, P. Walter, G. Blobel, Protein translocation across the endoplasmic reticulum. II. Isolation and characterization of the signal recognition particle receptor. *J. Cell Biol.* **95**, 470–477 (1982).

69. E. Nir, X. Michalet, K. M. Hamadani, T. A. Laurence, D. Neuhauser, Y. Kovchegov, S. Weiss, Shot-noise limited single-molecule FRET histograms: Comparison between theory and experiments. *J. Phys. Chem. B* **110**, 22103–22124 (2006).

70. K. Zhang, Gctf: Real-time CTF determination and correction. *J. Struct. Biol.* **193**, 1–12 (2016).

71. J. Zivanov, T. Nakane, B. O. Forsberg, D. Kimanius, W. J. H. Hagen, E. Lindahl, S. H. W. Scheres, New tools for automated high-resolution cryo-EM structure determination in RELION-3. *eLife* **7**, e42166 (2018).

72. A. Brown, S. Shao, J. Murray, R. S. Hegde, V. Ramakrishnan, Structural basis for stop codon recognition in eukaryotes. *Nature* **524**, 493–496 (2015).

73. P. D. Adams, P. V. Afonine, G. Bunkóczi, V. B. Chen, I. W. Davis, N. Echols, J. J. Headd, L. W. Hung, G. J. Kapral, R. W. Grosse-Kunstleve, A. J. McCoy, N. W. Moriarty, R. Oeffner, R. J. Read, D. C. Richardson, J. S. Richardson, T. C. Terwilliger, P. H. Zwart, PHENIX: A comprehensive Python-based system for macromolecular structure solution. *Acta Crystallogr. D Biol. Crystallogr.* **66**, 213–221 (2010).

74. E. F. Pettersen, T. D. Goddard, C. C. Huang, G. S. Couch, D. M. Greenblatt, E. C. Meng, T. E. Ferrin, UCSF Chimera—A visualization system for exploratory research and analysis. *J. Comput. Chem.* **25**, 1605–1612 (2004).

75. T. D. Goddard, C. C. Huang, E. C. Meng, E. F. Pettersen, G. S. Couch, J. H. Morris, T. E. Ferrin, UCSF ChimeraX: Meeting modern challenges in visualization and analysis. *Protein Sci.* **27**, 14–25 (2018).

76. W. L. DeLano, The PyMOL Molecular Graphics System, Version 2.3. *Schrödinger LLC* (2020); http://www.pymol.org.